Supporting Information

Mapping Short-Range Order at the Nanoscale in Metal–Organic Framework and Inorganic Glass Composites

Joonatan E. M. Laulainen*[a], Duncan N. Johnstone[a], Ivan Bogachev[a], Louis Longley[a], Courtney Calahoo[b], Lothar Wondraczek[b], David A Keen[c], Thomas D. Bennett[a], Sean M. Collins*[a,d], and Paul A. Midgley*[a].

a. Department of Materials Science and Metallurgy, University of Cambridge, 27 Charles Babbage Road, Cambridge CB3 0FS, UK

b. Bragg Centre for Materials Research, School of Chemical and Process Engineering and School of Chemistry, University of Leeds, Leeds LS2 9JT, UK

c. Otto Schott Institute of Materials Research, Friedrich Schiller University Jena, Fraunhoferstrasse 6, 07743 Jena, Germany.

d. ISIS Facility, Rutherford Appleton Laboratory, Harwell Campus, Didcot OX11 0QX, UK

Contents:

1. **SED data pre-processing and calibration**

SED data were acquired using a Merlin-Medipix3 hybrid counting-type direct electron detector. The data were acquired with either a 512×512 pixel quad Medipix3 detector or a single 256×256 pixel Medipix3.

Calibration of the scan step size and diffraction pattern pixel size was performed using a standard 500 nm gold diffraction grating replica with latex spheres (Ted Pella). The gold diffraction data was also used to determine residual elliptical distortions in the diffraction plane due to post-specimen optics.

The SED data was pre-processed in Pyxem as follows:
1. Centering the direct beam in each diffraction pattern using a cross-correlation routine.
2. Applying an affine transformation to correct for elliptical distortion.
3. Integrating each diffraction pattern azimuthally around the center of the direct beam to acquire a 1D scattering profile.

2. X-ray scattering acquisition

X-ray data were collected at the I15-1 beamline at Diamond Light Source, UK ($\lambda = 0.161669$ Å, 76.7 keV). Samples were loaded in borosilicate capillaries of 1.17 mm inner diameter. Data were collected in the region of ~$0.4 < Q < $ ~22 Å^{-1}. Correction for the background, multiple scattering, container scattering, Compton scattering, fluorescence and absorption were performed using the GudrunX program [1].
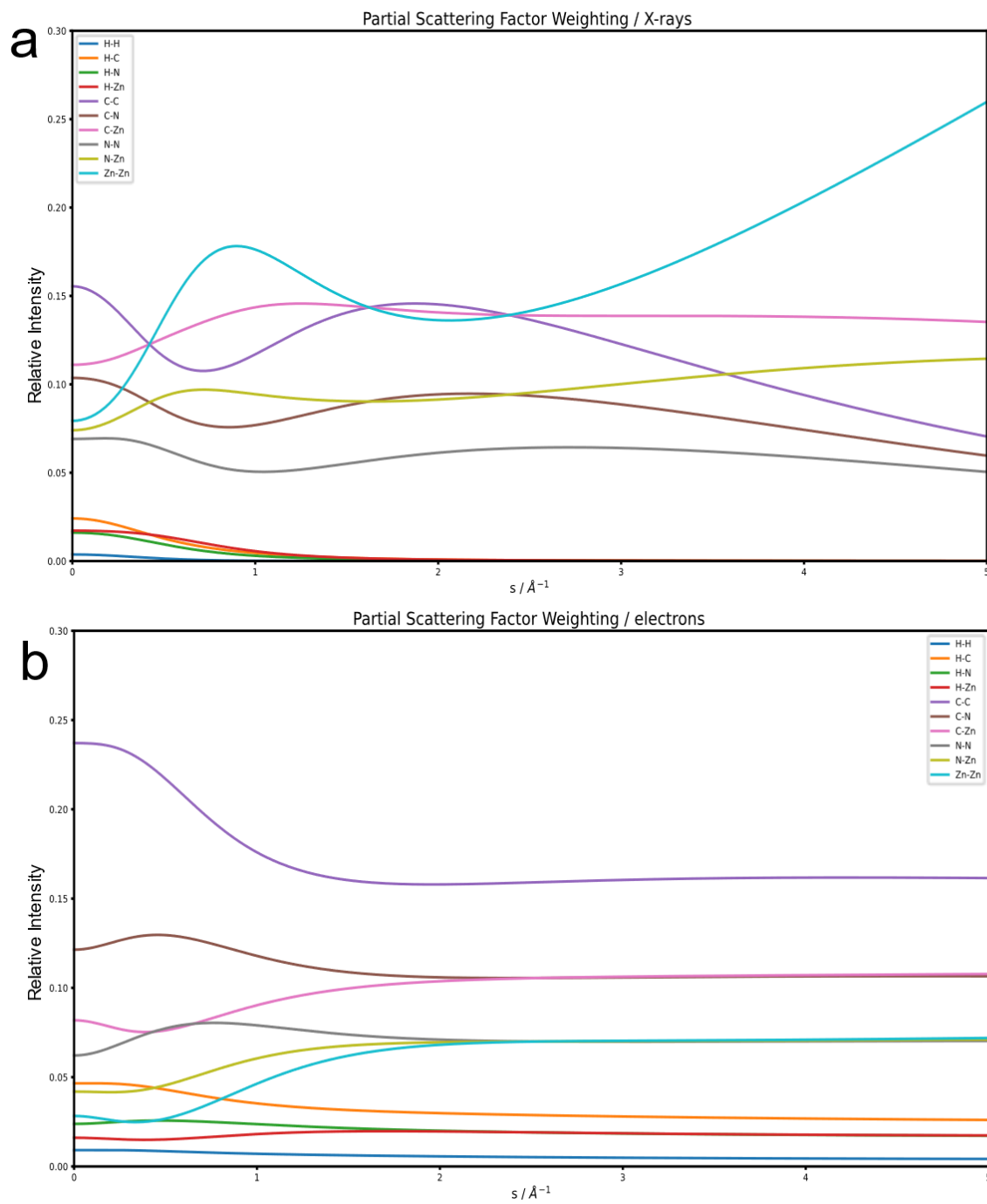
3. Relative Electron and X-ray Scattering factors

The relative scattering factors by element differ between X-ray and electron scattering. The pair partial scattering factors $f_{\alpha\beta}(s)$ are given by[2]

$$f_{\alpha\beta}(s) = \frac{c_\alpha c_\beta f_\alpha(s) f_\beta(s)}{\left[\sum_{i=1}^{n} c_i f_i(s)\right]^2}$$

where $\sum_{i=1}^{n} c_i f_i(s)$ is the sum over all elements n in the sample and a $f_\alpha(s)$ is the scattering factor for element α. Note that due to the division by the total sum, the relative contribution of a pair can increase with increasing s, even though $f_\alpha(s)$ is a decreasing function. The factors[3] and their relative ratios are plotted below for ZIF-62 in Figures S1 and S2 respectively. In particular, the significant relative increase in IX-H correlations at high s is notable (Fig. S2), primarily due to the extremely low scattering cross-section of H by X-rays. In electron scattering in absolute rather than relative terms (Fig. S1b), the H contribution is relatively weak, but it is non-negligible
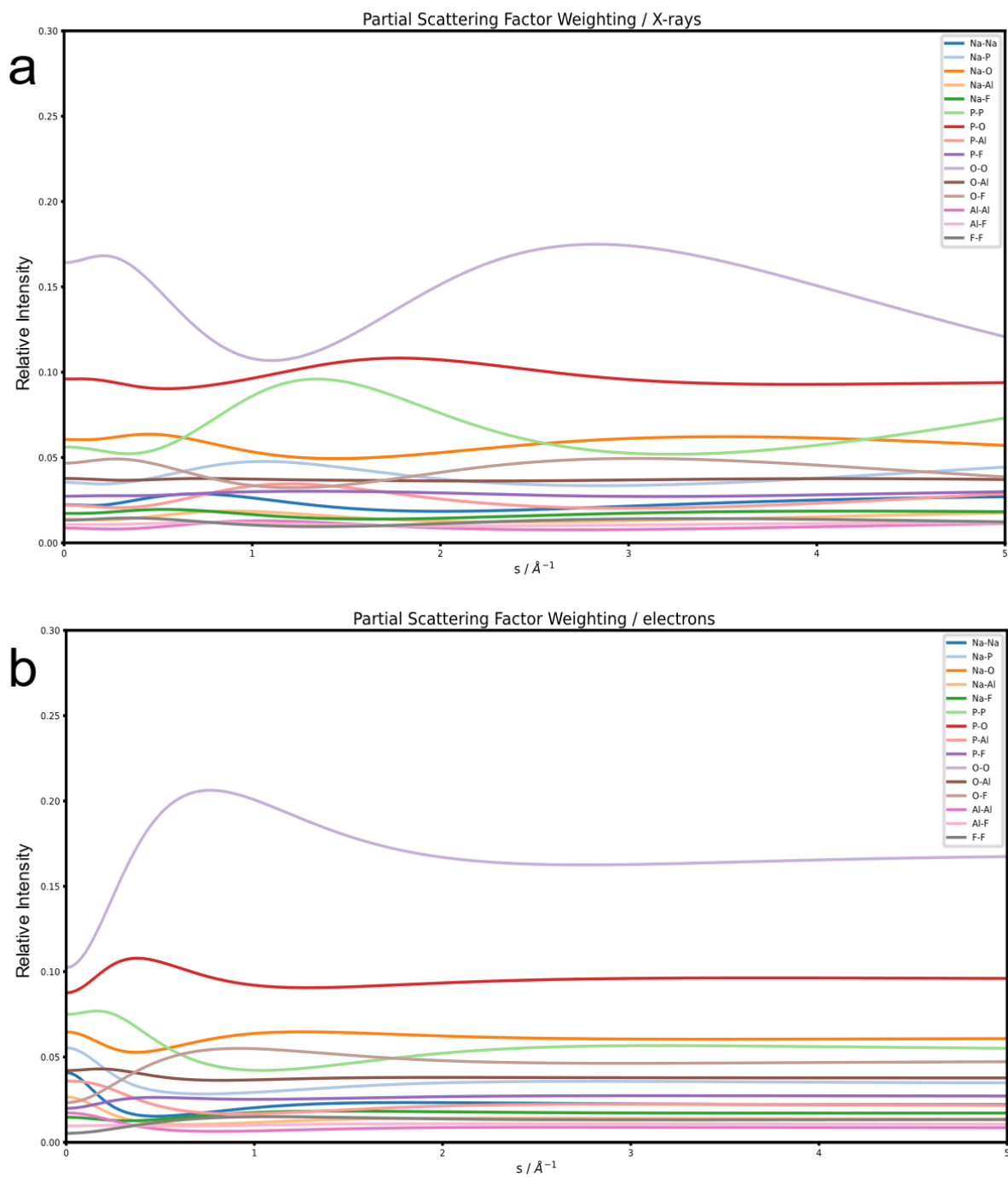
The relative scattering factors for the inorganic glass are given in Figures S3 and S4. The fractional changes are much smaller as there is no H involved. F-F, O-F, and O-O partials are strengthened around 0.7 Å^{-1} where two peaks showed inversion in the reduced intensity, and P-P, P-Al, and Al-Al partials are particularly reduced.

Figure S1. Pair partial (a) X-ray and (b) electron and scattering factors for the composition of ZIF-62 used as a function of scattering vector s for $0 < s < 5$ Å^{-1}.
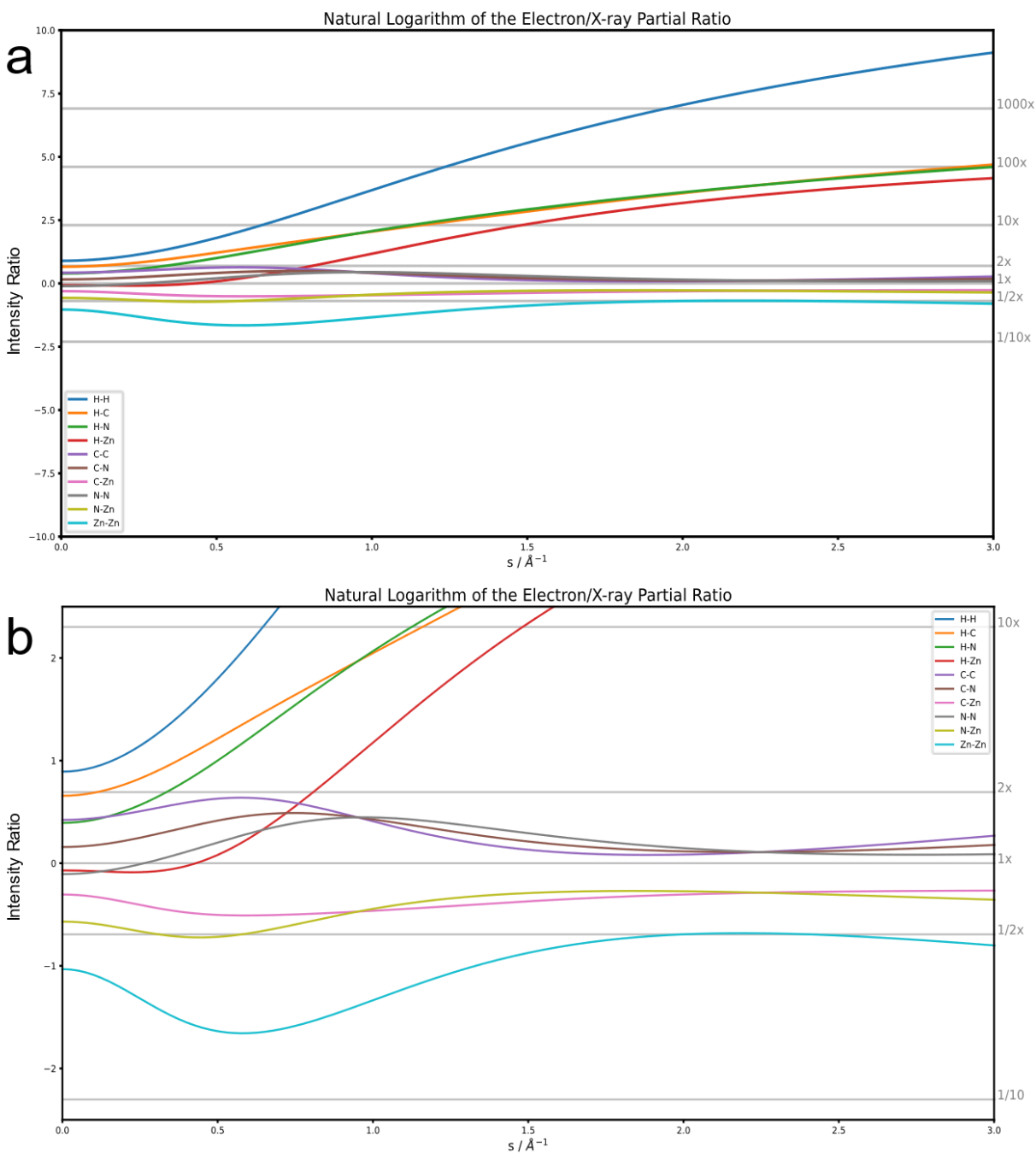
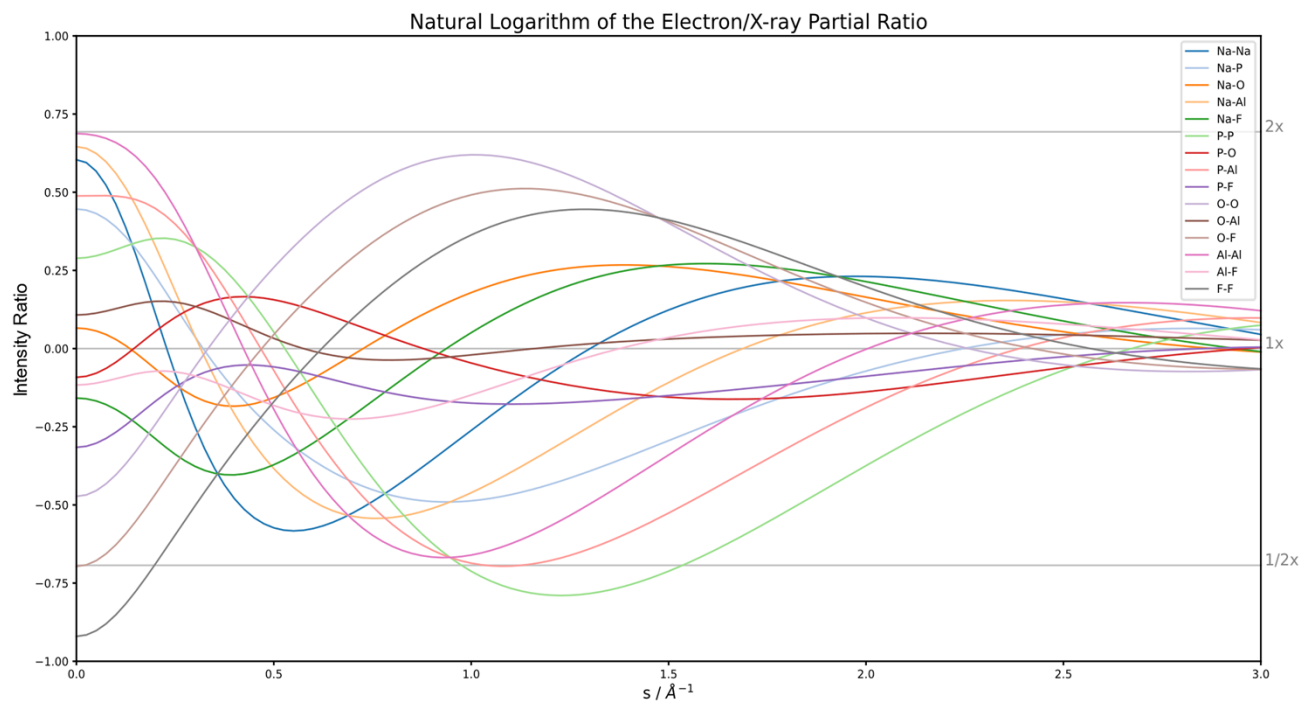**Figure S2.** The natural logarithm of the electron/X-ray pair partial ratio for ZIF-62 as a function of s for the partials given in Figure S1 for $0 < s < 3$ Å^{-1}. (a) Full scale and (b) inset to show the non-H terms.

Figure S3. Pair partial (a) X-ray and (b) electron and scattering factors for the composition of inorganic glass used as a function of scattering vector s for $0 < s < 5$ Å^{-1}.

Figure S4. The natural logarithm of the electron/X-ray pair partial ratio for inorganic glass as a function of s for the partials given in Figure S1 for $0 < s < 3$ Å^{-1}. The overall scale of difference is much smaller than in the ZIF-62.

4. Crystalline ZIF-62 PDF fitted with electron and X-ray scattering factors

A simplified ZIF-62 crystal structure was used to calculate partial atomic pair distribution functions, which were then turned into partial reduced intensities and multiplied by the partial scattering factor distributions given above in Figures S1.

The ZIF-62 crystal structure retrieved from the Cambridge Structural Database (CSD, CCDC number 671070) incorporates disorder in the benzimidazolate (bIm) position as well as solvent molecules[4]. For ZIF-62 PDF calculations, a lowered symmetry structure was adapted from the same lattice parameters and derived from the fractional coordinates of the reported ZIF-62 structure, with partial occupancies and solvent molecules removed (Table S1). This approach is similar to that used by Thorne *et al.*[5] though here we retain all hydrogen atoms in the structure.

The same data processing pipeline as for the respective X-ray and electron data was followed, and are presented in Figure S5a-b. The differences in the simulated electron and X-ray PDFs are very consistent with the observed differences, with the relative intensities of the 5 and 6 Å peaks accurately represented. The inaccuracies in peak intensities between simulated and observed PDFs is likely due to the lack of bIm$^-$ linkers in the unit cell.

In addition, Figure S5c-f contain simulated electron and X-ray PDFs for a range of S_{max} values. The same processing was applied to each PDF, to ensure any differences are due to different scattering factors. The partial structure factors were obtained, weighted, and damped by a Lorch function before being transformed into reduced PDF. Relative peak intensities differ throughout, but in a consistent manner. Peaks around 1.0, 1.5 Å and 5 Å are stronger in ePDF, while peaks are 2.6, 3.1, 4.9, and 6.4 Å are stronger in XPDF. Many of the distances stronger in the ePDF are associated with H, such as C-H and Zn-H partial[6]. This suggests the difference in the electron and X-ray PDFs observed in Figure 2 are real features that are differentially weighted in electron and X-ray scattering.

Table S1. Fractional coordinates for $P2_12_12_1$ (space group 19) unit cell (a = b = 15.662 Å, c = 18.207 Å) created to idealize the ZIF-62 structure for PDF calculations.

| Atom label	x	y	z	Atom label	x	y	z
C1	0.1091	0.1149	0.5986	N8	0.0637	0.2364	0.6451
C2	0.1006	0.04	0.5491	ZN1	0.30343	0.13921	0.59659
H2	0.1489	0.0166	0.5297	ZN2	0.49743	0.16499	0.31671
C3	0.0207	0.009	0.537	ZN3	0.00257	0.66499	0.31671
H3	0.0155	0.9567	0.5133	ZN4	0.19657	0.63921	0.59659
C4	0.9472	0.0503	0.5578	C17	0.3909	0.6149	0.5986
H4	0.8941	0.0267	0.5475	H17	0.3905	0.56	0.5791
C5	0.9541	0.1353	0.5978	C18	0.4633	0.66	0.6172
H5	0.9065	0.1686	0.6085	H18	-0.4806	0.6415	0.6115
C6	0.0367	0.16	0.6172	C19	0.1184	0.8154	0.613
C7	0.3816	0.3154	0.613	H19	0.1372	0.8363	0.5681
H7	0.3628	0.3363	0.5681	C20	0.1857	0.5143	0.7217
C8	0.3143	0.0143	0.7217	H20	0.2304	0.5387	0.748
H8	0.2696	0.0387	0.748	C21	0.212	0.587	0.437
C9	0.288	0.087	0.437	H21	0.2652	0.5611	0.4417
H9	0.2348	0.0611	0.4417	C22	0.0993	0.6518	0.4578
C10	0.4007	0.1518	0.4578	H22	0.0566	0.6819	0.4822
H10	0.4434	0.1819	0.4822	C23	0.1671	0.5937	0.374
C11	0.3329	0.0937	0.374	H23	0.1842	0.5729	0.3285
H11	0.3158	0.0729	0.3285	C24	0.092	0.7358	0.7022
C12	0.408	0.2358	0.7022	H24	0.0898	0.6876	0.7319
H12	0.4102	0.1876	0.7319	C25	0.0743	0.8598	0.6641
C13	0.4257	0.3598	0.6641	H25	0.0583	0.9168	0.6604
H13	0.4417	0.4168	0.6604	C26	0.1363	1.4507	0.7461
C14	0.3637	0.9507	0.7461	H26	0.1395	1.4251	0.792
H14	0.3605	0.9251	0.792	C27	0.0978	1.4853	0.6396
C15	0.4022	0.9853	0.6396	H27	0.0675	1.4874	0.5957
H15	0.4325	0.9874	0.5957	C28	0.3517	0.7348	0.6391
C16	0.1483	0.2348	0.6391	H28	0.3175	0.7809	0.6523
H16	0.1825	0.2809	0.6523	N9	0.3199	0.6627	0.613
N1	0.1801	0.1627	0.613	N10	0.1302	0.7362	0.6382
N2	0.3698	0.2362	0.6382	N11	0.1615	0.538	0.6542
N3	0.3385	0.038	0.6542	N12	0.1677	0.6238	0.4923
N4	0.3323	0.1238	0.4923	N13	0.0943	0.6352	0.3876
N5	0.4057	0.1352	0.3876	N14	0.0574	0.8079	0.7209
N6	0.4426	0.3079	0.7209	N15	0.0802	1.4299	0.6915
N7	0.4198	0.9299	0.6915	N16	0.4363	0.7364	0.6451
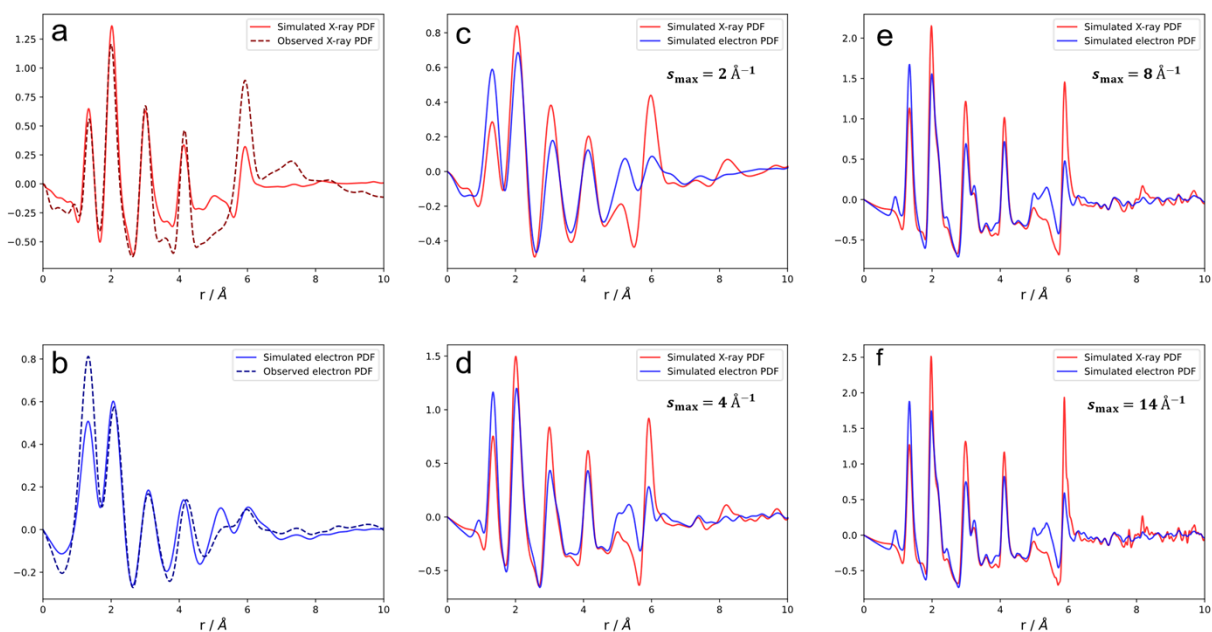
Figure S5. (a) Simulated and observed XPDFs from Figure 2 of the described ZIF-62 unit cell, with the same processing conditions for each (b) The simulated and observed ePDFs, again following the same processing conditions. (c)-(f) Simulated X-ray (red) and electron (blue) PDFs for a given s_{max} using a Lorch function for damping. The s_{max} ranges from 2 Å^{-1} (c) to 14 Å^{-1} (f) (13 Å^{-1} to 88 Å^{-1} equivalent Q_{max}.

5. ZIF-62 PDF as a function of maximum scattering vector

The area-averaged PDFs from the a_gZIF-62 were fitted with varying strength of damping factor b for the $\exp(-bs^2)$ term to investigate whether the feature around 5 Å is a result differing scattering factors. The resulting PDFs are shown in Figures S1. The feature was present until a high damping factor, like features around 7 Å and the major peaks around 2-3 Å. It changes faster than peaks at low r but similarly to the features around it. A fit similar fit was performed with just changing s_{min} and s_{max}, shown in Figure S6. Little changes were observed. While it is not possible to conclusively rule out the feature as a result of a truncation effect, its lack of change suggests it may be a structural feature.
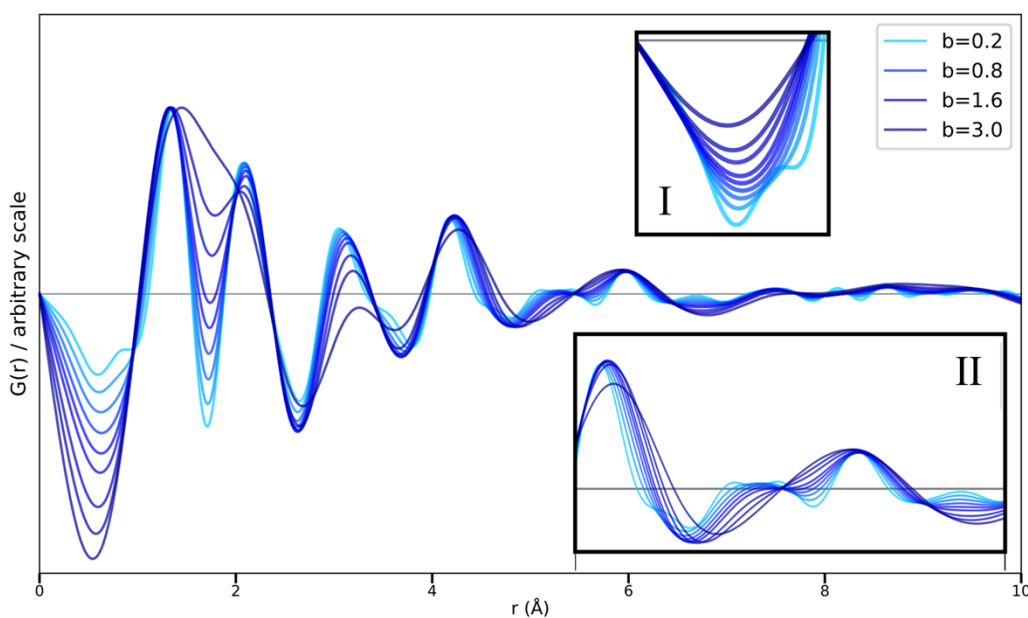

Figure S6. a_gZIF-62 PDF as a function of damping factor b, rescaled to the height of the first peak. **I**: Inset showing $G(r)$ at low r without rescaling. **II**: Inset showing the $4 < r < 7$ Å in more detail. The feature is present until a damping factor of 3.
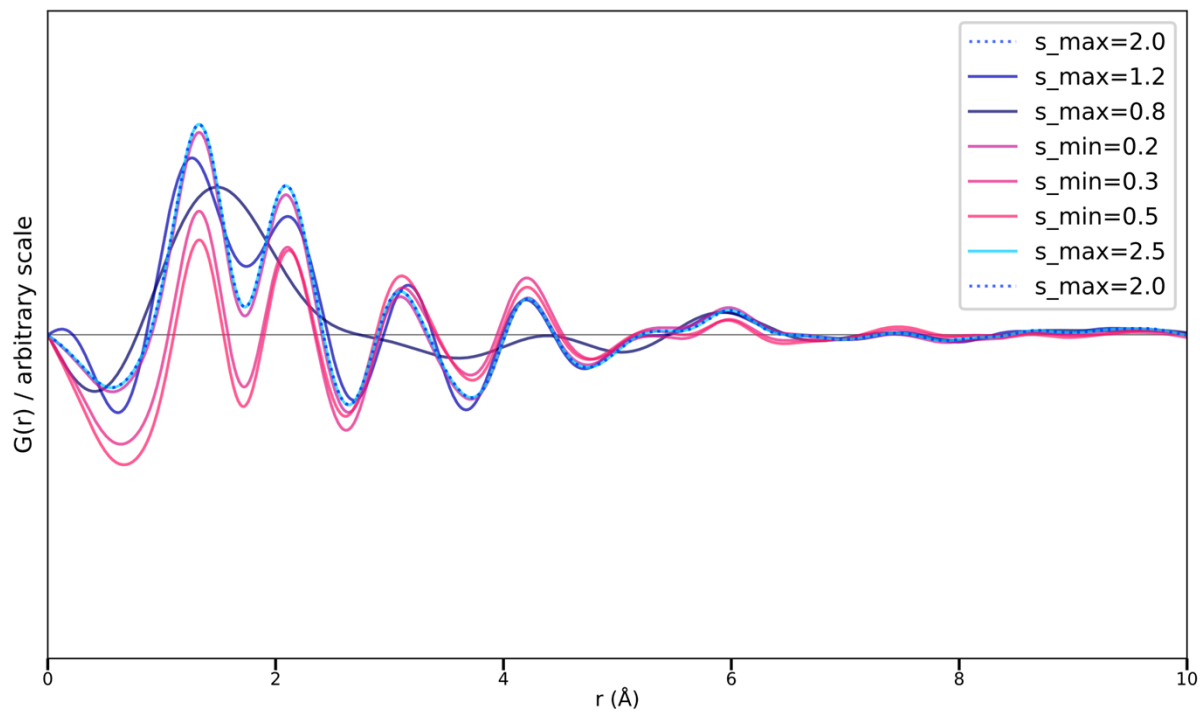
Figure S7. a_gZIF-62 ePDF variation as a function of s_{min} and s_{max}. Blue: reducing s_{max}, Red: Increasing s_{min}.

6. Principal Component Analysis Variance ratios

For each PCA decomposition, the component-variance ratios were used to choose the number of signal components for the subsequent ICA decomposition. Two significant components were chosen for the decompositions in both Figure 3 and Figure 5. The variance ratios by component are presented below.
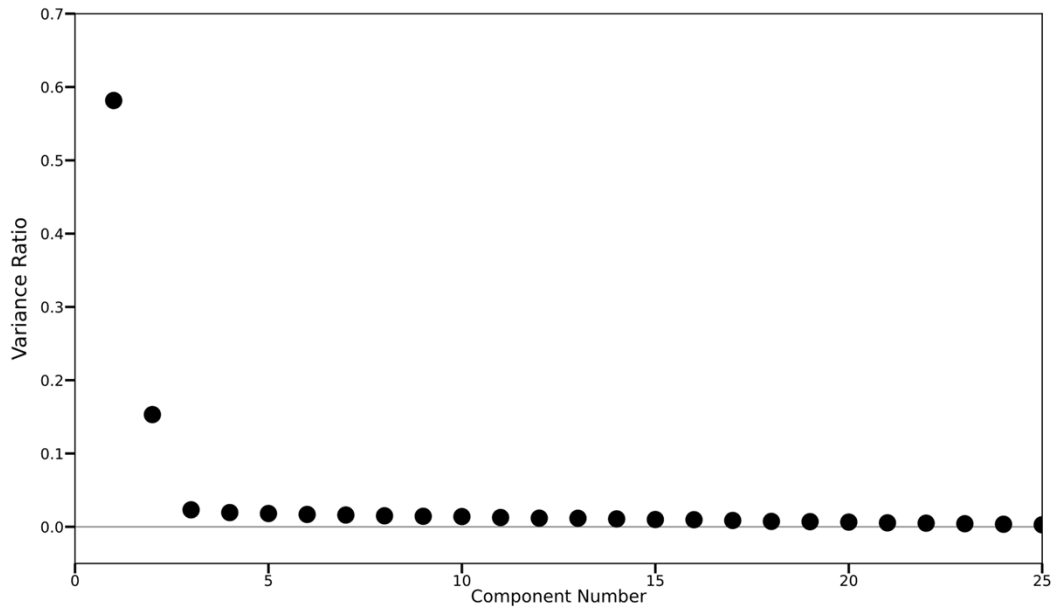

Figure S8a. Fraction of the variance explained by the most significant 25 principal components. The PCA decomposition was performed on the pixel-by-pixel ePDFs for the 512×512 data set shown in Figure 3. Two components are strongly above the baseline and were used for the subsequent ICA decomposition.
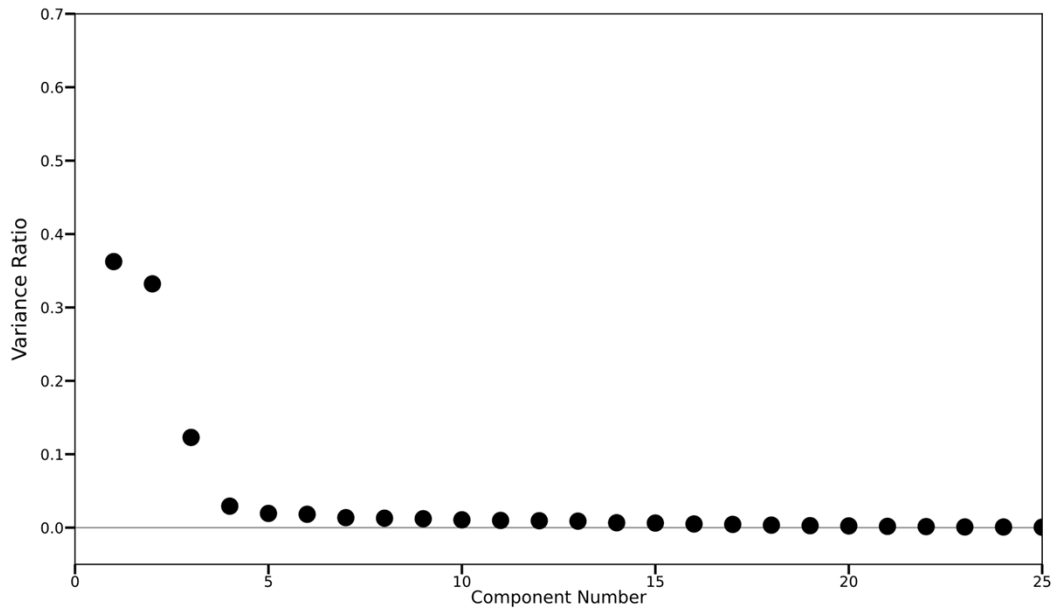
Figure S8b. Fraction of the variance explained by the most significant 25 principal components. The PCA decomposition was performed on the pixel-by-pixel ePDFs for the 256×256 data set shown in Figure 5. Three components were above the baseline, but the largest two that were significantly higher were used for the subsequent ICA decomposition. The third was not found to contain meaningful spatial variation information and reduced the accuracy of the two PDFs compared to the higher fidelity 512×512 data set.
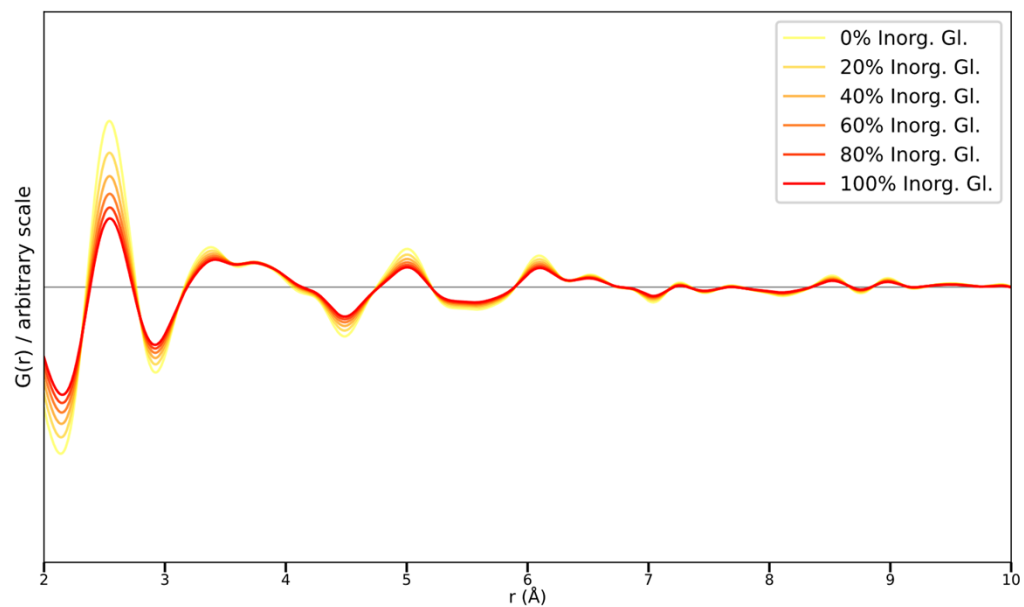
7. PDF as a function of background composition

The area-averaged PDFs from the a_gZIF-62 and inorganic glass were fitted with varying background compositions. The fits are shown in Figures S9a and S9b. The effect of an incorrect composition was primarily to increase peak heights in the a_gZIF-62 and decrease peak heights in the inorganic glass. This can be attributed to the different scattering profile being fit as a function of composition, combined with incorrect fitting at low s as a result of inelastic scattering. Peak positions were virtually unchanged, meaning incorrect background fitting should have little to no effect on the ICA decomposition being able to distinguish the signals from one another.
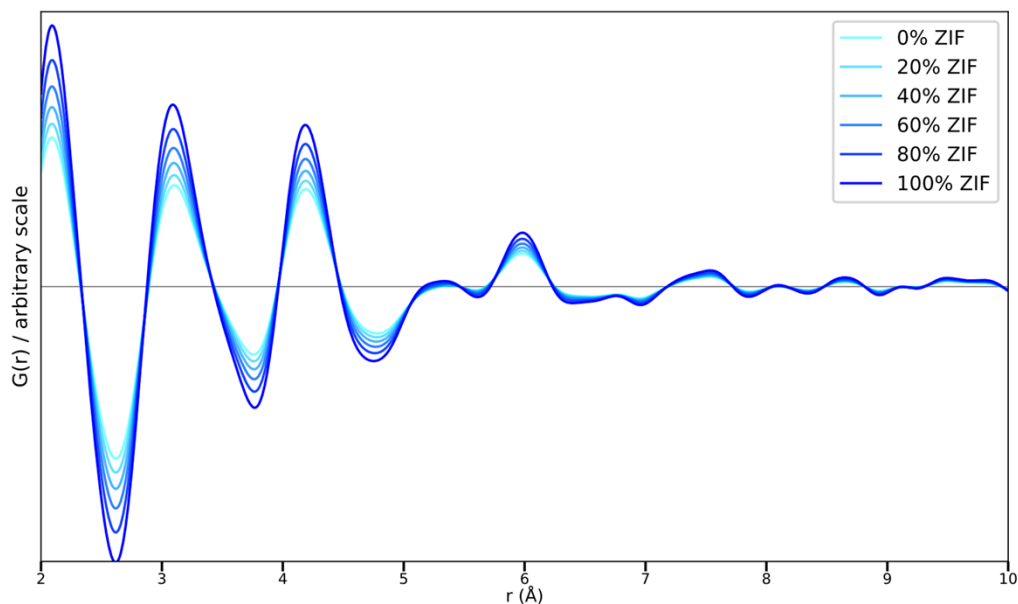

Figure S9a. Area-averaged ePDF as a function of background composition for the a_gZIF-62, from 100% a_gZIF-62 and 0% inorganic glass to 0% a_gZIF-62 and 100% inorganic glass.

Figure S9b. Area-averaged ePDF as a function of background composition for the inorganic AlF_3-$NaPO_3$ glass, from 100% inorganic glass and 0% a_gZIF-62 and to 0% inorganic glass and 100% a_gZIF-62.

8. PDF of carbon film

An ePDF was acquired from the carbon film to compare to references. The reduced intensity and PDF profiles are plotted below in Fig S3a and S3b. The ePDF agrees well with previous works[7], with peak positions at 1.4 Å and 2.5 Å accurately reflected. In general, the carbon signal is very weak in comparison to the nanoparticles. Notably, the ICA in Figure 3 showed incomplete separation of the ePDFs at approximately 2.5 Å which may be related to the amorphous carbon contributions from the support film.
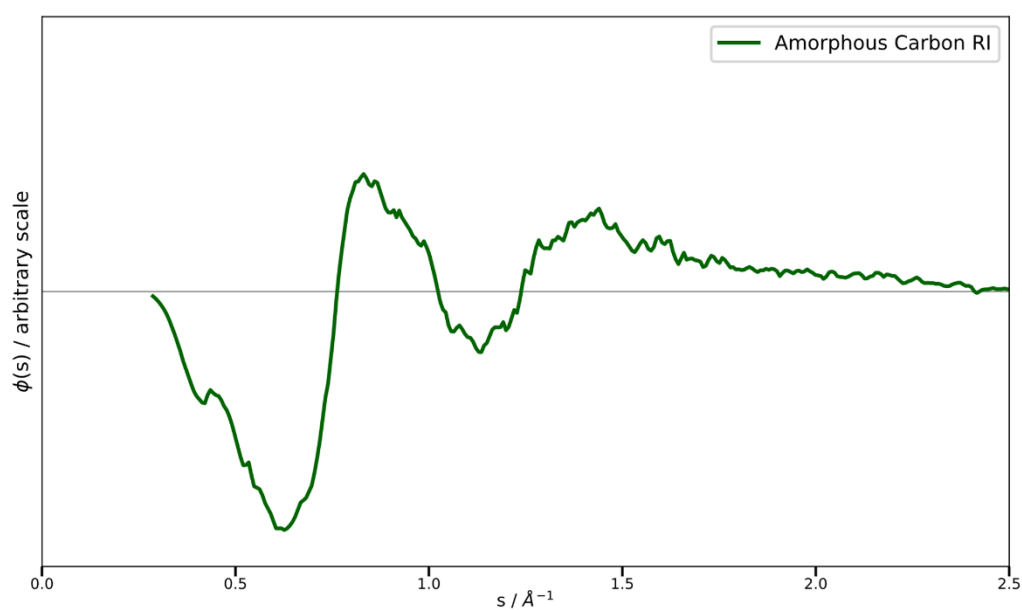

Figure S10a. Reduced intensity measured in the carbon film, averaged from a 50×50-pixel real space region.
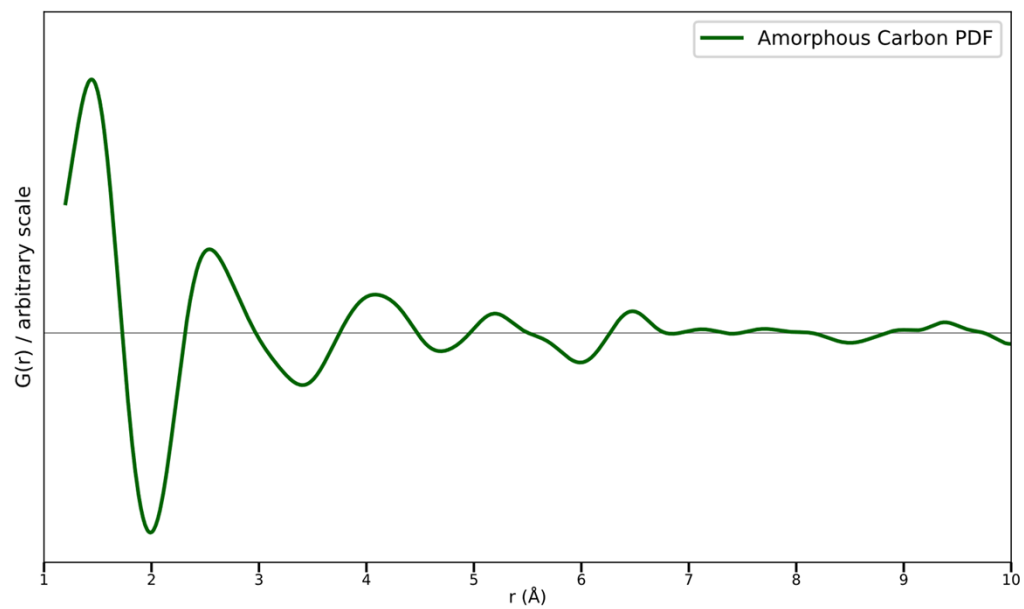
Figure S10b. STEM-ePDF of the amorphous carbon film, from the reduced intensity in Fig S3a. The data was summed from a 50×50-pixel real space region.

9. PDF variation across thickness

The variation of the acquired ePDFs as a function of thickness was investigated for both the a_gZIF-62 and the inorganic glass (Figure S1). The average peak height decreased with increasing thickness, but the peak positions remained consistent as expected[8]. Minor peak shifts were observed for the inorganic glass, likely due to its greater density and scattering power, resulting in fast changes with increased thickness relative to a_gZIF-62. The consistency in peak position and profile shape is important for the PCA/ICA decomposition as it should primarily affect the total weight of each phase assigned to each pixel, but not result in pixels being misclassified as one phase over the other. At large thicknesses, particularly in the inorganic glass, this assumption is no longer satisfied, but the primary peak positions are still well defined.
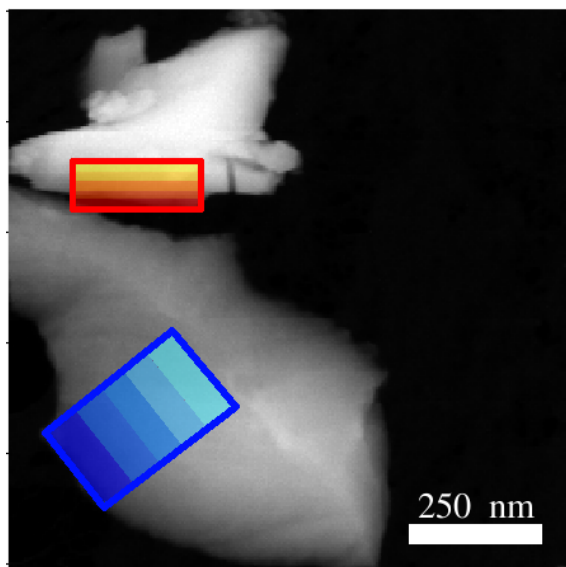
Figure S11a. Regions from which the thickness series were taken, overlaid on the ADF image from Figure 1.
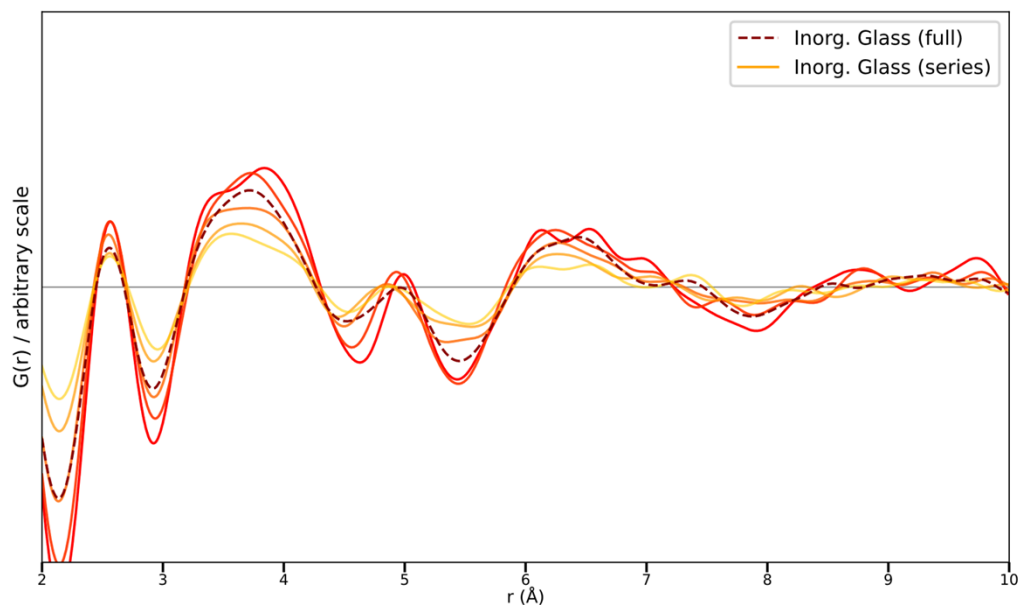
Figure S11b. A series of ePDFs acquired at different thicknesses of the inorganic NaPO$_3$-AlF$_3$ glass from the area shown in Figure S11a, overlaid with the area-averaged ('full') ePDF shown in Figure 2. Color coding follows Figure S11a. With increasing thickness (more yellow), the peaks become weaker and more blurred, with notable slight shifting and blurring of the peaks around 3.8 Å and 5 Å. The area-averaged PDF sits roughly in the middle of this thickness range
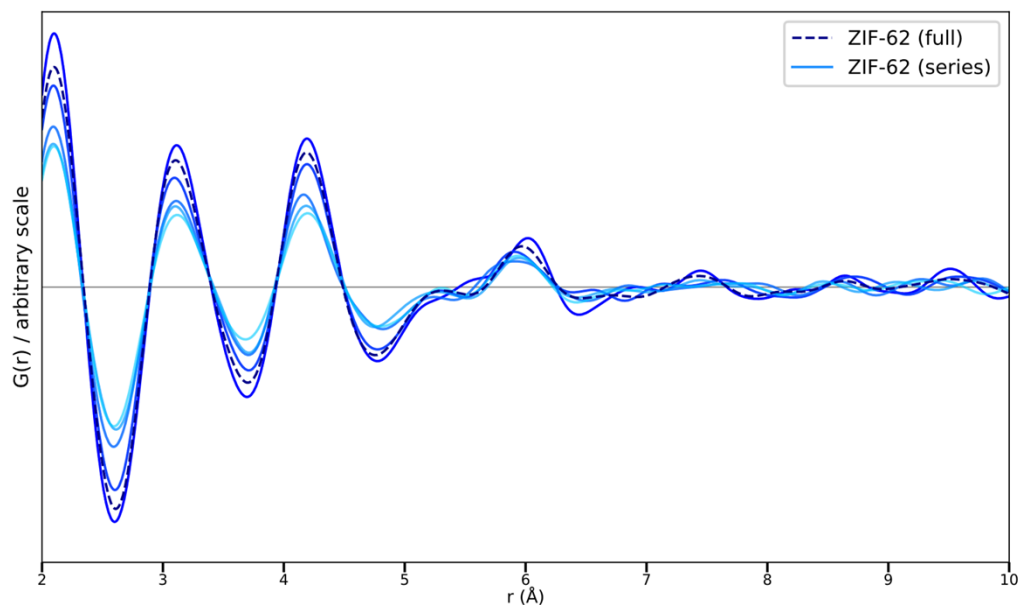
Figure S11c. A series of ePDFs acquired at different thicknesses of the a_gZIF-62 particle from the area shown in Figure S11a, overlaid with the area-averaged ('full') ePDF shown in Figure 2. Color coding follows Figure S11a. With increasing thickness (lighter blue), the peaks also become weaker and more blurred, although less so than the inorganic glass. The area-averaged PDF reflects the PDF from the thin areas more accurately.

## 10. ICA-PDF for the 256x256 pixel data set in Figure 5
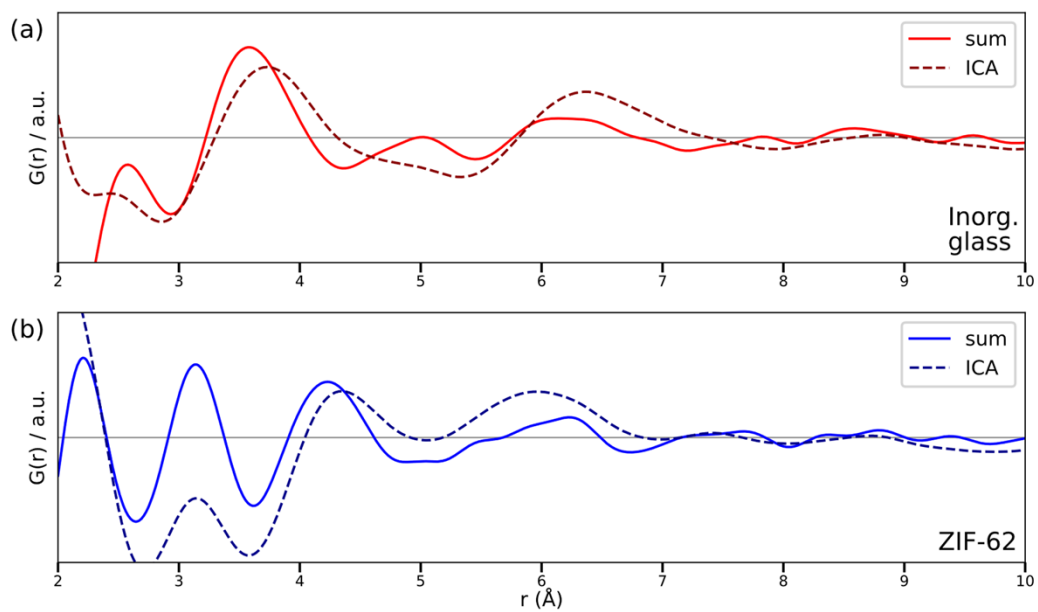
Figure S12. (a),(b) ICA component profiles and area corresponding area-averaged ePDFs for (a) the inorganic glass and (b) a_gZIF-62 in the 256x256 pixel data set used in Figure 5.

11. PDF at interfacial region

A PDF was acquired from the area at the interface outlined in purple in Figure S13 by summing the diffracted intensity and then performing the ePDF acquisition procedure detailed in the Methods. The acquired ePDF was compared to ones acquired from single-domain regions. These PDFs are show in Figure S13b. The interface PDF shows small differences to a best fit of a sum of the component PDFs, shown in Figure S13c. Small differences are present in relative peak intensities, but it was not possible to distinguish signal from noise in this interface signal.
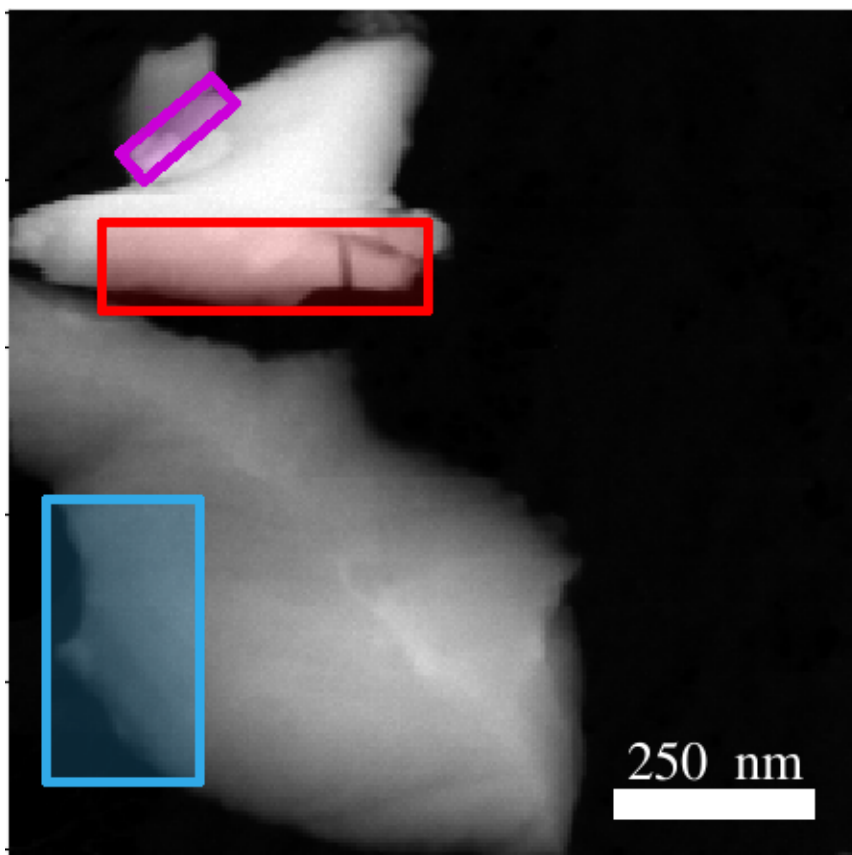
Figure S13a. Areas from which single domain ePDFs were calculated for the inorganic glass (red), a_gZIF-62 (blue), and the interface (purple).
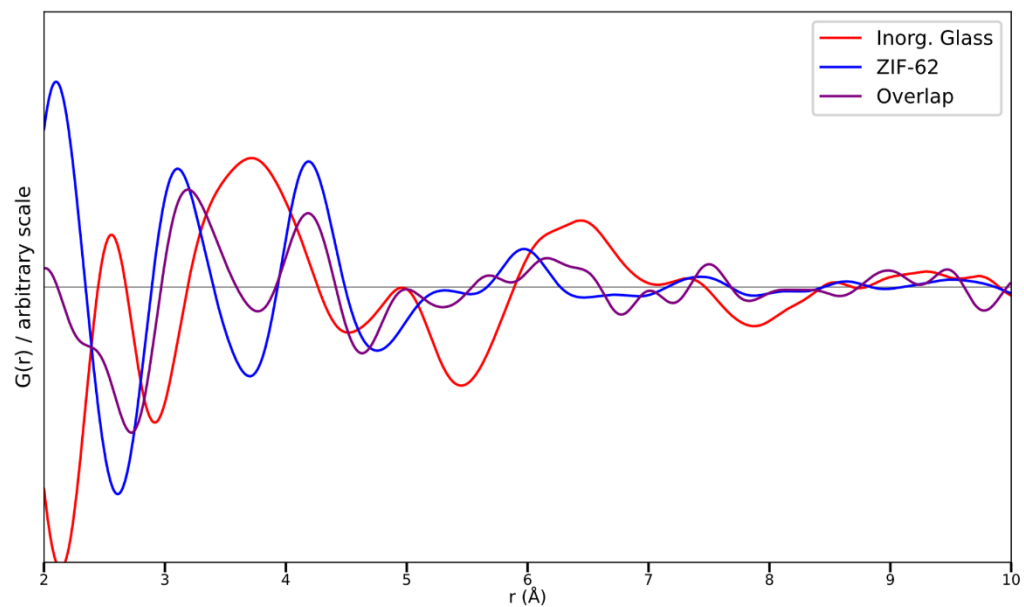
Figure S13b. The single-domain and interface region ePDFs. The diffraction profiles were summed before an ePDF was extracted for each of the signals. A weighted average scattering factor was used for fitting at the interface.
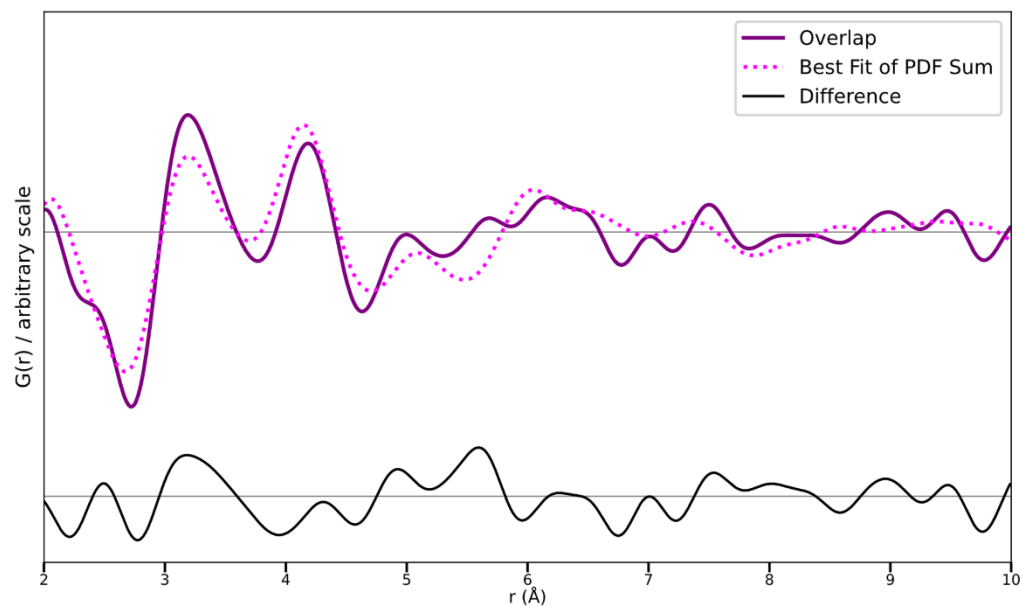
Figure S13c. The best fit of a sum of the red and blue ePDFs in Figure S13b, compared to the ePDF in the overlap region. Peak positions are reproduced, but relative height differ slightly. A difference is plotted at the bottom.

12. ICA decomposition of the reduced intensities

The PCA-ICA decomposition was also applied on the reduced intensities in the data set. This revealed two main components, but those components, particularly the inorganic glass, were significantly affected by thickness, as shown in Figure S14. A third component was observed above the noise floor, but not found to correspond to a physical signal and was instead partially correlated to thickness. Hence 2 components were used for the subsequent ICA decomposition. This thickness-dependent variation is a slow oscillation that manifests itself differently in the PDF, in a way that ICA was able to resolve, and as such ICA was directly applied to the PDF signals.
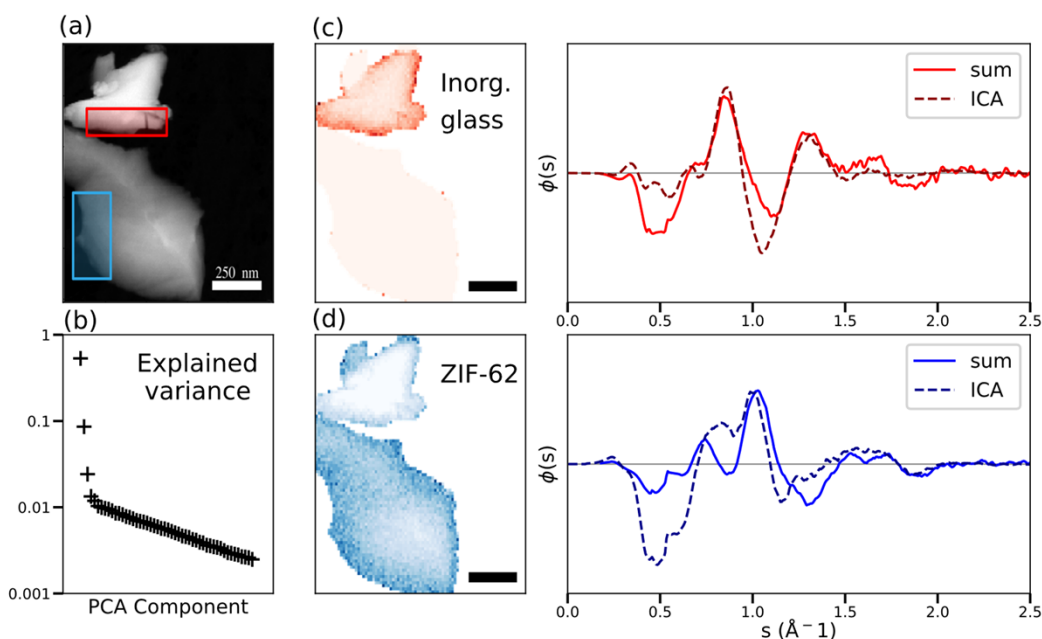
Figure S14. (a) ADF of the particles used in the main text. All scale bars 250 nm. (b) Explained variance of the PCA decomposition of the spatially-resolved reduced intensity $\phi(s)$. Two components were used for the subsequent ICA decomposition. (c), (d) the ICA loading maps of the two components. (e), (f) The ICA components of the two phases, compared to the area-averaged reduced intensities used in Figure 2.

References

(1)   Soper, A. K. GudrunN and GudrunX: Programs for Correcting Raw Neutron and X-Ray Diffraction Data to Differential Scattering Cross Section. *Rutherford Applet. Lab. Tech. Reports* **2011**, *RAL-TR-201*.

(2)   Egami, T.; Billinge, S. J. L. *Underneath the Bragg Peaks: Structural Analysis of Complex Materials*; Elsevier, 2003.

(3)   Lobato, I.; Van Dyck, D. An Accurate Parameterization for Scattering Factors, Electron Densities and Electrostatic Potentials for Neutral Atoms That Obey All Physical Constraints. *Acta Crystallogr. Sect. A Found. Adv.* **2014**, *70* (2014), 636–649. https://doi.org/10.1107/S205327331401643X.

(4)   Banerjee, R.; Phan, A.; Wang, B.; Knobler, C.; Furukawa, H.; O'Keeffe, M.; Yaghi, O. M. High-Throughput Synthesis of Zeolitic Imidazolate Frameworks and Application to CO_2 Capture. *Science (80-.).* **2008**, *319* (5865), 939–943.

(5)   Thorne, M. F.; Sapnik, A. F.; McHugh, L. N.; Bumstead, A. M.; Castillo-Blas, C.; Keeble, D. S.; Lopez, M. D.; Chater, P. A.; Keen, D. A.; Bennett, T. D. Glassy Behaviour of Mechanically Amorphised ZIF-62 Isomorphs. *Chem. Commun.* **2021**, *57* (73), 9272–9275.

(6)   Xiong, M.; Zhao, X.; Yin, G.; Ching, W. Y.; Li, N. Unraveling the Effects of Linker Substitution on Structural, Electronic and Optical Properties of Amorphous Zeolitic Imidazolate Frameworks-62 (a-ZIF-62) Glasses: A DFT Study. *RSC Adv.* **2020**, *10* (24), 14013–14024. https://doi.org/10.1039/c9ra09977h.

(7)   Marks, N.; McKenzie, D.; Pailthorpe, B.; Bernasconi, M.; Parrinello, M. Ab Initio Simulations of Tetrahedral Amorphous Carbon. *Phys. Rev. B - Condens. Matter Mater. Phys.* **1996**, *54* (14), 9703–9714. https://doi.org/10.1103/PhysRevB.54.9703.

(8)   Anstis, G. R.; Liu, Z.; Lake, M. Investigation of Amorphous Materials by Electron Diffraction—The Effects of Multiple Scattering. *Ultramicroscopy* **1988**, *26* (1–2), 65–69.